

VIP Very Important Paper



Room Temperature Phase Transition in Methylammonium Lead Iodide Perovskite Thin Films Induced by Hydrohalic Acid Additives

Chan Myae Myae Soe,^[a, b] Constantinos C. Stoumpos,^[a] Boris Harutyunyan,^[b, c] Eric F. Manley,^[a, b, d] Lin X. Chen,^[a, b, d] Michael J. Bedzyk,^[b, c] Tobin J. Marks,^{*[a, b]} and Mercuri G. Kanatzidis^{*[a, b]}

Although reactive additives have been employed in perovskite solar cells to enhance film morphology and significantly increase device performance, little is known about the effect of these additives on perovskite structural and optical properties. Here we report a systematic study of how the properties of methylammonium lead iodide perovskite ($\text{CH}_3\text{NH}_3\text{PbI}_3$) are influenced by hydrohalic acid additives (HX; X = I, Br, Cl) in the precursor solution. Detailed structural and optical spectroscopic analysis reveals that all three acids affect the optical properties and alter the unit cell lattice parameters. Depending on the identity and concentration of HX, optical bandgaps widen or compress: addition of HBr yields a wider bandgap, whereas HI compresses the gap at high concentrations; HCl, on the other hand, has no significant effect on the bandgap. These

changes can be understood by correlating them with the types of defects present in polycrystalline perovskite thin films in combination with the structural strain induced in very small crystallites. The presence of extra halides from HX in the precursor solution enables filling of the lattice vacancies in the perovskite, thereby altering metal–halogen–metal bond connectivity and consequently cell volumes and optical bandgaps. Remarkably, a room temperature tetragonal→cubic phase transition is observed for $\text{CH}_3\text{NH}_3\text{PbI}_3$ films treated with high HX concentrations. Further insights into this anomalous phase transformation are obtained from in situ variable-temperature X-ray diffraction in the 25–55 °C (298–328 K) range, revealing a monotonic fall in transition temperature with increasing precursor solution HX concentration.

Introduction

Methylammonium lead iodide perovskite ($\text{CH}_3\text{NH}_3\text{PbI}_3$) and related halide perovskites were recently shown to function as

superb light-harvesting materials for photovoltaic applications.^[1–13] They are dramatically changing solar cell technology, despite being newcomers, owing to their excellent intrinsic semiconducting properties and long carrier diffusion lengths, combined with facile and versatile solution processability. Perovskite solar cells have yielded remarkable power conversion efficiencies (PCEs), comparable to established thin-film photovoltaic materials, such as copper indium gallium selenide (CIGS) and cadmium telluride (CdTe). Since the emergence of perovskite solar cells, research efforts have focused on improving the film morphology as well as charge extraction layers and device architecture, resulting in PCEs surging to as high as 22.1% within a five-year period. Attempts to control perovskite film morphology have yielded diverse fabrication protocols, which can be categorized as: i) one-step solution methods,^[9,11] ii) vapor-assisted solution processes,^[14,15] iii) sequential deposition,^[16] iv) dual vapor deposition,^[17] and v) hot-casting.^[18]

The one-step solution methodology involves simple spin-casting from a solution of precursor salts, followed by low temperature annealing; in principle, the simplicity and low material and fabrication cost makes this method attractive for commercialization. However, one-step spin-coating from stoichiometric precursor salts typically results in unfavorable discontinuous, rough film morphologies with poor surface coverage. Within the one-step processing concept, efforts to overcome this

[a] C. M. M. Soe, Dr. C. C. Stoumpos, E. F. Manley, Prof. L. X. Chen, Prof. T. J. Marks, Prof. M. G. Kanatzidis
Department of Chemistry
Northwestern University
Evanston IL, 60628 (USA)
E-mail: t-marks@northwestern.edu
m-kanatzidis@northwestern.edu

[b] C. M. M. Soe, B. Harutyunyan, E. F. Manley, Prof. L. X. Chen, Prof. M. J. Bedzyk, Prof. T. J. Marks, Prof. M. G. Kanatzidis
Argonne-Northwestern Solar Energy Research Center
Northwestern University
Evanston, Illinois 60208 (USA)

[c] B. Harutyunyan, Prof. M. J. Bedzyk
Departments of Physics and Astronomy and Materials Science and Engineering
Northwestern University
Evanston, Illinois 60208 (USA)

[d] E. F. Manley, Prof. L. X. Chen
Chemical Sciences and Engineering Division
Argonne National Laboratory
9700 S. Cass Ave., Lemont, IL 60439 (USA)

Supporting Information for this article can be found under:
<http://dx.doi.org/10.1002/cssc.201600879>.

This publication is part of a Special Issue focusing on the “Stability of Perovskite Solar Cells and Devices”. To view the Complete issue, visit:
<http://onlinelibrary.wiley.com/doi/10.1002/cssc.v9.18/issuetoc>.

issue include: (1) composition engineering,^[19,20] (2) solvent-engineering,^[21–23] (3) tuning annealing conditions,^[24,25] and (4) incorporating additives. The role of additives extends beyond improving film morphology because additives can also enhance precursor salt solubility, particularly of metal halides in organic solvents. To date, several additives have been explored for this purpose: organic small molecules, such as 1,8-diiodooctane^[26] and 1,3-bis[3,5-di(pyridin-3-yl)phenyl]benzene,^[27] halide salts, such as $\text{CH}_3\text{NH}_3\text{Cl}$ ^[28] and NH_4Cl ,^[29] and interestingly, strong acids, such as HI ^[30,31] and HCl ,^[32] affording PCEs as high as 15% from simple one-step spin-casting, followed by brief annealing times.

We were particularly intrigued by the application of strong acid additives to tune perovskite film morphology because excess halide represents a natural additive that in principle offers the potential to easily tune crystal growth and defect levels. Furthermore, the substantial change in deposition solution pH from slightly basic, in solvents such as dimethylformamide (DMF), offers a tunable parameter for enhancing device performance. Despite enhanced morphology and PCE, little is understood about the effects of excess halides on perovskite electronic and crystal structure. Thus, it would be desirable to obtain a fundamental understanding of the interplay between processing parameters and perovskite properties by synthesizing these materials in highly acidic precursor environments. The reactive nature of HI was demonstrated by Xiao and coworkers, where they reported the synthesis of a new precursor, HPbI_3 , obtained by precipitating PbI_2 from a concentrated aqueous HI solution.^[33] There, the HI incorporation led to approximately 15% PCE. With all of these factors taken into account, it is clearly important to understand how HX additives interact with perovskites.

In this study, we investigate the impact of employing strong HX additives on the growth and properties of $\text{CH}_3\text{NH}_3\text{PbI}_3$ films. A systematic study is conducted in which small increments of concentrated, aqueous HI, HBr, and HCl solutions are incorporated in the stoichiometric $\text{CH}_3\text{NH}_3\text{I}/\text{PbI}_2$ DMF precursor solutions, followed by simple one-step thin-film fabrication. Remarkably, these additives yield subtly different $\text{CH}_3\text{NH}_3\text{PbI}_3$ phases at room temperature depending on the HX concentration: the expected tetragonal β -phase is obtained at low acid concentrations, whereas the more symmetrical pseudocubic α -phase is obtained at high acid concentrations. In the absence of additives, this transition is known to occur at approximately 57 °C both in the bulk material and in thin films.^[34–35] To better understand this unusual behavior, detailed investigations of perovskite optical bandgaps and structural properties (lattice constants and phase transition temperature) are carried out as a function of HX identity and concentration. This phase transition can be understood in terms of the strain induced on the structure at very small grain sizes while the observed trends in optical and structural properties can be rationalized by changes in defect density in the thin films and “self-healing” effects associated with the presence of extra halide, which counterbalances the inherent defects in perovskite thin films.

Results and Discussion

Perovskite crystal structure

Halide perovskites of the form AMX_3 , where $\text{A}^+ = \text{Cs}^+$, CH_3NH_3^+ , $\text{HC}(\text{NH}_2)_2^+$; $\text{M}^{2+} = \text{Ge}^{2+}$, Sn^{2+} , Pb^{2+} ; and $\text{X}^- = \text{Cl}^-$, Br^- , I^- , adopt high symmetry crystal structures in which $[\text{MX}_6]^{4-}$ octahedra are corner-connected in all directions to form a 3D framework. The self-assembly of the anionic inorganic $[\text{MX}_3]^-$ framework generates cuboctahedral cages containing the A^+ cations.^[36] For ideal cubic symmetry, all $\text{M}-\text{X}-\text{M}$ bond angles are 180°, and the cage is perfectly symmetrical, resulting in strong orbital overlap between metal cations and halide anions. Deviations from the ideal cubic phase arise when the $\text{M}-\text{X}-\text{M}$ bond angles diverge from 180° in the ab plane, affecting the orbital overlap. Such scenarios occur when the perovskite is subjected to heat^[37] and/or pressure,^[13,34,38] resulting in contraction or expansion of the $[\text{MX}_3]^-$ framework. Thus, perovskites with $\text{M}-\text{X}-\text{M}$ angles as low as 150° exist at low temperatures.^[4] However, when the $\text{M}-\text{X}-\text{M}$ angle is 150°, the perovskite structure is no longer stable and collapses to a different structure type or becomes amorphous.^[4,13,34] In the case of hybrid organic–inorganic halide perovskites (e.g., $\text{CH}_3\text{NH}_3\text{PbI}_3$), the highest symmetry crystal structure is pseudocubic (α -phase, $P4mm$ space group) as a result of the asymmetric cation shape, even though it might be argued that the structure is still macroscopically cubic because the cations are in a state of dynamic disorder.^[37,39] At room temperature, $\text{CH}_3\text{NH}_3\text{PbI}_3$ deviates from the pseudocubic phase because the CH_3NH_3^+ cation is slightly below the ideal size to fit in the fully extended $[\text{PbI}_3]^-$ cage; the perovskite structure is stabilized by tilting the octahedra to 163.6° along the crystallographic ab plane, increasing the density and yielding the tetragonal symmetry β -phase, $I4cm$ space group (Figure 1). In $I4cm$ the normalized a and b axes ($a = a^* \times \sqrt{2}$; $b = b^* \times \sqrt{2}$) expand along the tetragonal plane, whereas the normalized c axis ($c = c^* \times 2$) contracts with respect to the primitive $P4mm$ cell ($a^* = b^* \approx c^*$). X-ray diffraction (XRD) and calorimetric measurements indicate that $\text{CH}_3\text{NH}_3\text{PbI}_3$ undergoes a tetragonal \rightarrow cubic phase transition between 42 and 57 °C,^[39–41] where thermal expansion and

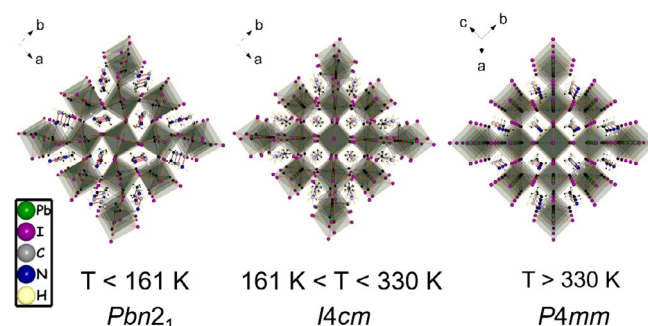


Figure 1. $\text{CH}_3\text{NH}_3\text{PbI}_3$ phase transition sequence. At high temperatures, it crystallizes in the pseudocubic phase ($P4mm$ space group). Upon cooling, it transforms into the tetragonal structure ($I4cm$ space group) at approximately 330 K. Lowering the temperature further results in an additional phase transition to the orthorhombic phase ($Pbn2_1$ space group) at around 160 K.^[34]

Pb–I bond vibrations force the opening of the Pb–I–Pb angle back to approximately 180° (Figure 1). In the pseudocubic phase, while the cell volume contracts, the organic cation is accommodated in the octahedral cage due to the rapid, thermally activated rotation of the organic cation.^[42] Upon cooling, thermal motion is suppressed, and the organic cation motion freezes below approximately 160 K, resulting in further distortion of the metal–halide cage and adoption of orthorhombic space group $Pbn2_1$.^[37] Further cooling to cryogenic temperatures leads to complete cation immobilization, which takes place in an incoherent fashion, yielding a perovskite “glass”.^[43] This phase behavior is intrinsic; however, it appears that external chemical factors, such as additives used during thin-film deposition from the solution, can dramatically influence the perovskite’s properties.

Thin-film growth and properties

Perovskite films were fabricated by spin-coating DMF solutions containing a stoichiometric ratio of $\text{CH}_3\text{NH}_3\text{I}$ and PbI_2 , to which differing measured concentrations of aqueous HX (X = I, Br, Cl) were systematically added. Unlike neutral additives, acidic additives can interact with the DMF solvent, disrupting the strong hydrogen bonding between solvent molecules and between solvent molecules and CH_3NH_3^+ cations, thereby lowering the solution viscosity. These changes in chemical environment significantly affect solvent properties, such as evaporation rate, a critical factor during spin-casting that determines the perovskite crystallization rate.^[44] Although the standard one-step fabrication procedure yields an intermediate red film, probably owing to the incompletely converted perovskite, upon annealing it converts to the black perovskite. In marked contrast, the present acid additives facilitate instantaneous formation of perovskite, as judged by the film color change to black immediately after spin-coating, but prior to thermal treatment. Enhanced crystallization rates have been suggested to be critical in fabricating high-quality perovskite films. To achieve this, Xiao et al. dripped chlorobenzene anti-solvent on the spinning film,^[23] whereas Nie et al. pre-heated the substrate to high temperatures prior to spin-casting.^[18]

Note that a striking improvement in film quality is observed only upon addition of acid as shown in Figure 2. The typical $\text{CH}_3\text{NH}_3\text{PbI}_3$ films from one-step spin-coating are dull dark brown in color with a typical root-mean-square (RMS) roughness of 110 nm. Top-view scanning electron microscopy (SEM) images of this control film reveal the typical needle-shaped morphology, unfavorable for photovoltaic properties, in agreement with the literature.^[28, 29, 32, 45] In contrast, the films fabricated using the acidic additives appear shinier and darker with a significant reduction in surface roughness ($\text{RMS} \approx 50$ nm). The darker perovskite color implies a qualitatively more compact film morphology with enhanced light absorption, a key factor for maximizing photocurrent. This dramatic improvement in film morphology upon HX incorporation is also evident in Figure 2, where more continuous and smoother polycrystalline films with fewer pinholes are obtained. Such morphologies are highly desirable for solar cell applications, espe-

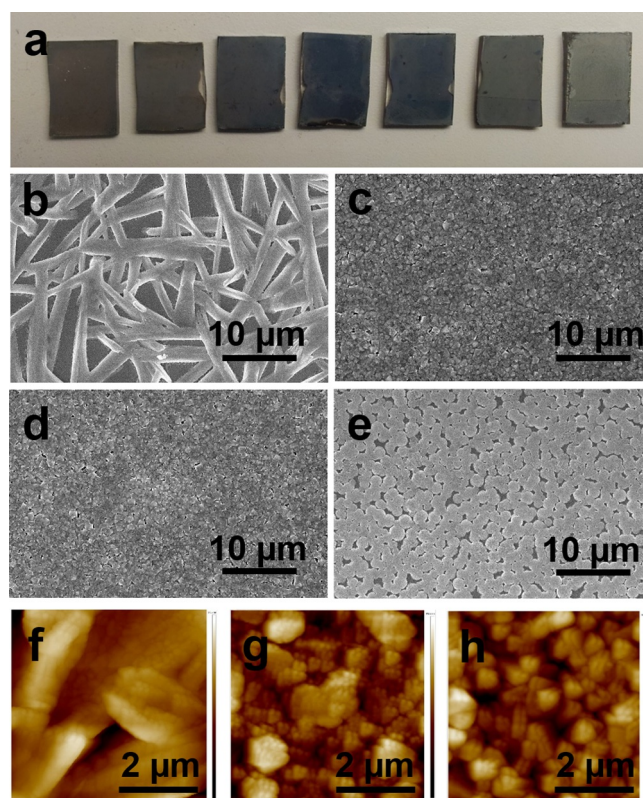


Figure 2. (a) Photographic images of films deposited with increasing HI concentrations in the DMF precursor solution. Left to right: 0, 2, 4, 6, 8, 10, and 15 vol% HI. Top-view SEM images of $\text{CH}_3\text{NH}_3\text{PbI}_3$ films on ITO/PEDOT:PSS spin-coated from stoichiometric $\text{CH}_3\text{NH}_3\text{I}/\text{PbI}_2$ precursor solutions, (b) without any additives and with 10 vol% of HX additives: (c) HI, (d) HBr, and (e) HCl. Representative AFM images of $\text{CH}_3\text{NH}_3\text{PbI}_3$ films, (f) without any additive, (g) with 5 vol% HI, and (h) 10 vol% HI. The size of the AFM images is $5 \times 5 \mu\text{m}^2$.

cially in planar device structures, to avoid direct contact of the two electrodes through pinholes, a shorting pathway that compromises cell performance.

X-ray diffraction analysis

The halide perovskite system is unique in that complex multi-step synthetic routes are unnecessary prior to device fabrication; $\text{CH}_3\text{NH}_3\text{PbI}_3$ synthesis simply takes place in situ on the substrate during annealing. To characterize the phase in the resulting HX-processed thin films, room-temperature powder XRD (PXRD) data were taken on spin-coated $\text{CH}_3\text{NH}_3\text{PbI}_3$ thin films fabricated from solutions with varied HI, HBr, and HCl concentrations. To calibrate the diffraction peaks and eliminate artifacts arising from inequivalent film/substrate thickness, poly(3,4-ethylenedioxythiophene):polystyrene sulfonate (PEDOT:PSS)-coated indium tin oxide (ITO) substrates were used with the ITO serving as an internal standard; a $\text{CH}_3\text{NH}_3\text{PbI}_3$ film without additive served as a control. As noted above, $\text{CH}_3\text{NH}_3\text{PbI}_3$ is known both experimentally and theoretically to crystallize in the $I4cm$ structure at room temperature and to transform to a more symmetric $P4mm$ pseudocubic phase

upon heating. This transition reportedly occurs at approximately 57 °C (330 K) and is reversible, with the tetragonal phase restored upon cooling back to room temperature.^[36] The simulated perovskite XRD patterns are shown in Figure S1. The (211) reflection at $2\theta = 23.54^\circ$ and the (022) reflection at $2\theta = 24.54^\circ$ are characteristic of the tetragonal phase and merge into the (111) reflection of the pseudocubic phase. As shown in Figure S2, the experimental data match the simulated diffraction patterns well for the tetragonal phase without detectable second phases, such as (i) PbI_2 , (ii) $\text{CH}_3\text{NH}_3\text{PbCl}_3$, and/or (iii) the yellow solvated $\text{CH}_3\text{NH}_3\text{PbI}_3\cdot\text{DMF}$ or $\text{CH}_3\text{NH}_3\text{PbI}_3\cdot\text{H}_2\text{O}$ phases.^[15,46] Despite achieving enhanced PCEs when these impurities are present,^[16,18] their role is not fully understood. A brief identification of the aforementioned second phases is summarized as follows: (i) the characteristic PbI_2 peak at $2\theta = 12.5^\circ$ is considered to reflect the incomplete conversion to perovskite as observed in sequential deposition processes or due to loss of $\text{CH}_3\text{NH}_3\text{I}$ and/or $\text{CH}_3\text{NH}_3\text{Cl}$ in the 3:1 $\text{CH}_3\text{NH}_3\text{I}/\text{PbCl}_2$ synthetic method,^[16-17,47] (ii) the $\text{CH}_3\text{NH}_3\text{PbCl}_3$ phase is observed in the synthesis of $\text{CH}_3\text{NH}_3\text{PbI}_2\text{Cl}^{[11]}$ when $\text{CH}_3\text{NH}_3\text{Cl}$ is used as the precursor salt,^[18,28] and (iii) the low angle peaks at $2\theta < 10^\circ$ are associated with the yellow perovskite phase that can arise from perovskite–solvent molecule hydrogen-bonding interactions, forming $\text{CH}_3\text{NH}_3\text{PbI}_3\cdot\text{Y}$ solvates ($\text{Y} = \text{H}_2\text{O}$, DMF, DMSO).^[15,22] Upon acid addition at low concentrations, the tetragonal structure is retained without detectable impurity peaks (Figure S2). However, at higher acid concentrations, certain tetragonal Bragg reflections disappear as a result of a tetragonal→cubic phase transition, with the most pronounced change occurring with the (211) reflection at $2\theta = 23.3^\circ$ [Note that the (211) peak in simulated XRD pattern is at a slightly higher 2θ of 23.54°]. To eliminate the possibility that the absence of the (211) reflection is a result of preferred orientation along the (022) plane, we state that in this case the (114), (222), and (310) reflections at $2\theta = 31.7^\circ$ should also vanish as shown in Figure S1; however, the PXRD of the thin films in our study (Figure S2) do not corroborate this statement, which confirms the observed phase transformation. In addition, the 2D grazing incidence wide angle X-ray scattering (GIWAXS) data further support the argument that orientational effects do not play a role here, as evidenced by the complete absence of the (211) reflection in the film treated with high acid concentration (Figure S3). The occurrence of this transition is quite remarkable because it is not a result of thermal activation. Formation of the $\text{CH}_3\text{NH}_3\text{PbI}_3$ perovskite cubic phase, normally a high-temperature process, occurs here at room temperature as a result of HX addition. Several reports claim the formation of the $\text{CH}_3\text{NH}_3\text{PbI}_3$ cubic phase at room temperature through a chloride-mediated phase transition.^[48,49] In the present study, such a phase transition is confirmed in detail and shown to apply to all $\text{CH}_3\text{NH}_3\text{PbI}_3$ films prepared from solutions containing HI, HBr, or HCl additives, implying that such a transition to the room temperature cubic phase is not halogen specific. Instead, composition and strain in the structure through small grain sizes appears to have a striking impact on the perovskite structural integrity, as discussed below.

To determine whether the phase transition is solely the result of HX additives, two control film synthesis/XRD experiments were conducted on: (i) acid-treated films without post thermal annealing, and (ii) films fabricated with water alone as the additive because HX in this study is in saturated aqueous solutions. Experiment (i) probes whether the phase transition is a result of thermal annealing or HX additive effects. Note from Figure S4 that the cubic phase is obtained even without thermal annealing, as evidenced by the absence of the (211) reflection at $2\theta = 23.3^\circ$. Additional peaks, however, are observed with added 20 vol% HI, likely reflecting solvent residues remaining in the film that form solvated iodoplumbates.^[50] In experiment (ii), the effects of water in the acid additives are probed by using water alone as an additive. While film XRD reflections associated with hydrated $\text{CH}_3\text{NH}_3\text{PbI}_3\cdot\text{H}_2\text{O}$ below $2\theta = 10^\circ$ and PbI_2 impurity at $2\theta = 12.5^\circ$ are detected upon adding up to 20 vol% water to the precursor solution, there is no effect on $I4cm$ perovskite structure formation (Figure S5). This implies that any water in the acid additive does not significantly contribute to the observed perovskite structural transition. From these control experiments, it is clear that the phase transition observed with HX additives is not a result of thermal activation, but is induced by the additives.

In addition to the phase transition, the PXRD data also reveal a shift in reflection positions with different HX concentrations, indicating changes in the unit cell dimensions (Figure 3). To accurately analyze these shifts and their structural consequences, pattern matching of the PXRD data was performed using Jana2006 Software,^[51] from which lattice parameters and unit cell volumes were extracted. For accurate determination of the cell volume, factors such as possible peak shifts induced by differences in sample heights were taken into account and normalized to the position of the ITO reflections. The structural trends vary with each HX additive, with HI and HCl exhibiting a marginal and slight increase in the unit cell volume, respectively, whereas HBr induces a decrease in the total volume, owing to the formation of the I/Br solid solution. Regarding the individual lattice parameters, an increase in the HI content tends to produce films with converging lattice parameters prior to the transition to the pseudocubic phase (Figure 3a). A similar trend is seen in HBr (Figure 3b), but upon addition of HCl, the dimensions of the a and c axes start to diverge, with both axes showing a small increase (Figure 3c). Note that these values are directly related to the nature of the acid since neutral water, used as a control, appears to have little effect on the perovskite unit cell (Figure 3d). Detailed discussions of these data are presented below.

To further examine the nature of the unusual phase transition, variable-temperature film XRD measurements were carried out with 2–3 °C step sizes. The series of thin films with HI was selected as representative (Figure 4). The temperature at which the characteristic (211) reflection of the $I4cm$ phase at $2\theta = 23.3^\circ$ disappears is considered the phase transition point in each case. Note that reflectivity values are background-subtracted. Reflectivity is a ratio of scattered and incident beam intensities, thereby independent of incident beam intensity variations from sample to sample. Error bars accounting

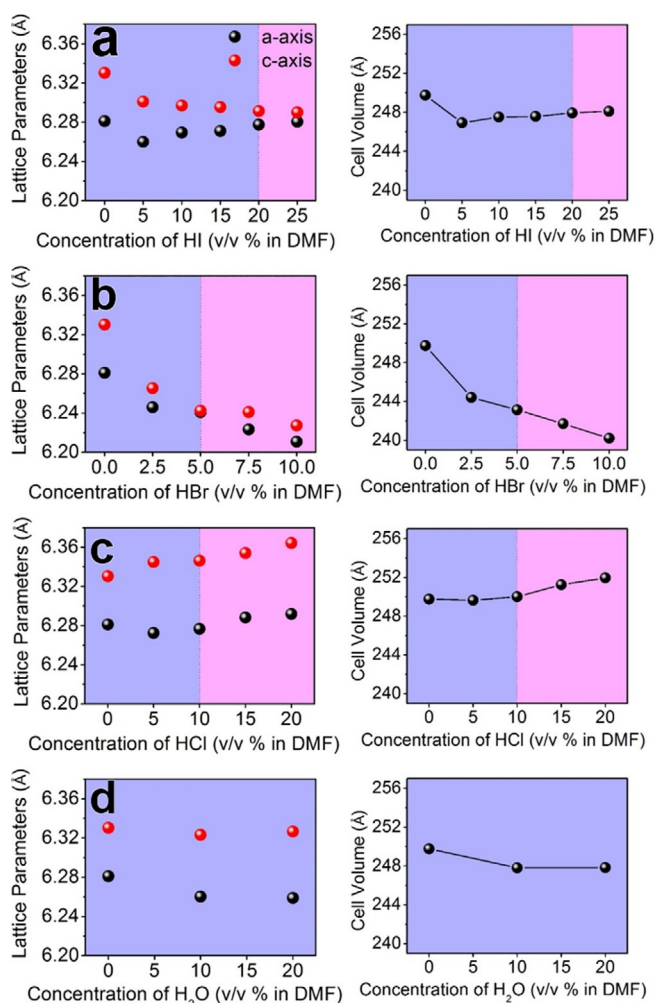


Figure 3. Unit cell volumes and lattice parameters of $\text{CH}_3\text{NH}_3\text{PbI}_3$ films on ITO/PEDOT:PSS substrates spin-coated from stoichiometric iodide precursor salt solutions, employing the indicated concentrations of (a) HI, (b) HBr, (c) HCl, and (d) H_2O as additives. The colored regions denote the conditions under which the tetragonal (blue) or the pseudocubic (pink) perovskite configuration is observed.

for count fluctuations (both in signal and subtracted background) in the point detector are obtained by Poisson statistics. As illustrated in Figure 4a, the effect is beyond the error bars and cannot be ascribed to statistical fluctuations. The control film without additive exhibits a phase transition near 61°C , very close to the reported value of 57°C .^[39–41] As seen in Figure 4, the transition shifts to lower temperatures as the HI concentration is increased, ultimately shifting to temperatures below the present instrumental range. This systematic decrease clearly demonstrates how HI addition gradually changes the perovskite crystal lattice and stabilizes the high-temperature cubic structure at room temperature at high acid concentrations.

Thin film optical absorption

The optical properties of the acid-treated perovskite films were next investigated to better understand the aforementioned

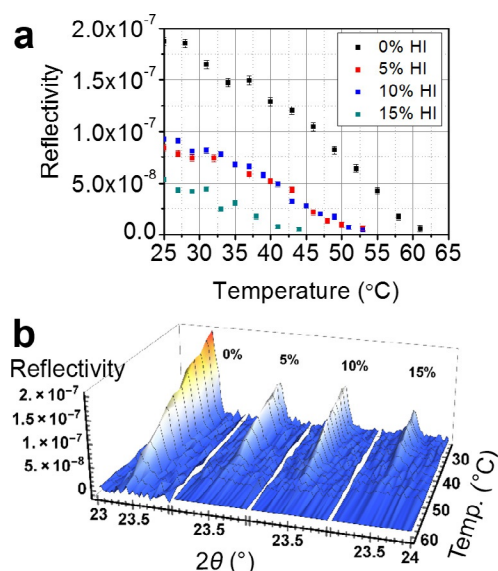


Figure 4. Devolution of the characteristic (211) reflection at $2\theta = 23.3^\circ$ for $\text{CH}_3\text{NH}_3\text{PbI}_3$ films prepared with the indicated HI concentrations as a function of temperature, indicating the $14cm \rightarrow P4mm$ phase transformation, (a) background-subtracted peak reflectivity (ratio between peak intensity and incident intensity) versus temperature, and (b) reflectivity at (211) peak as a function of scattering angle 2θ and temperature. The temperature at which the (211) reflection completely vanishes is considered a phase transition point.

structural transformations, and it is found that the optical bandgaps also change depending on the identity and concentration of HX additives. First, we briefly discuss the origin of the bandgap in $\text{CH}_3\text{NH}_3\text{PbI}_3$. The valence band is composed of Pb 6s and I 5p orbitals, and the bandwidth scales directly with the Pb–I–Pb bond angle.^[52] When this angle is 180° in the cubic structure, the orbital overlap between the metal and halide ions is maximum, yielding the smallest possible bandgap. When this angle deviates from linearity as in the tetragonal structure observed at room temperature, the orbital overlap falls, contracting the bandwidth and consequently widening the gap. As shown in Figures 5 and 6, a larger bandgap is observed with HBr, whereas the gap is marginally unchanged with HCl and 5–10 vol% HI and decreases at high HI concentrations. These effects are discussed in detail below.

(a) HI. HI is the simplest system and presumably only results in excess I^- in the precursor solution. Upon HI addition to $\text{CH}_3\text{NH}_3\text{PbI}_3$ precursor solutions, the film tetragonal unit cell expands along the ab plane in a linear fashion with respect to the amount of HI while contracting along the c axis (Figure 3a). The increasing ab plane and decreasing c axis gradually converge, smoothly transforming into the cubic phase at high HI concentrations; the phase transition occurs at room temperature for 20–25 vol% HI concentrations. Note that there is no significant change in the total unit cell volume with HI concentration (Figure 3a). Interestingly, there is only a marginal bandgap change at low HI concentrations (5–10 vol%), but the gap begins to fall beyond 10% (Figure 6a). The observed redshift in the bandgap in the cubic phase (20–25 vol% HI) with respect to the tetragonal phase is in accord with density func-

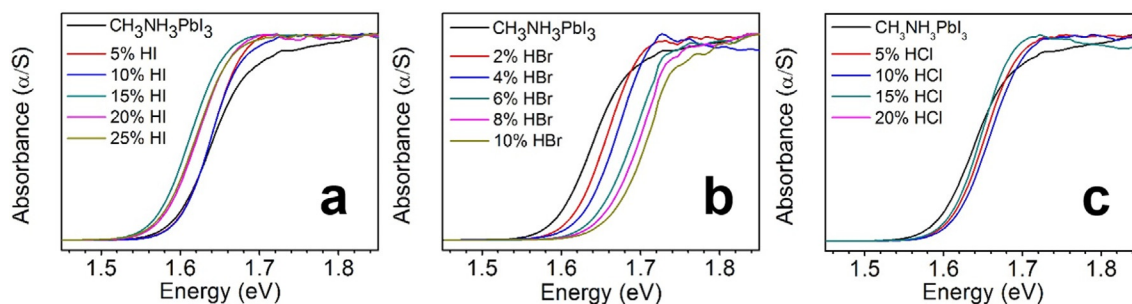


Figure 5. Optical bandgap determination for $\text{CH}_3\text{NH}_3\text{PbI}_3$ films on glass substrates spin-coated from stoichiometric $\text{CH}_3\text{NH}_3\text{I}/\text{PbI}_2$ precursor solutions with the indicated additive concentrations: (a) HI, (b) HBr, and (c) HCl.

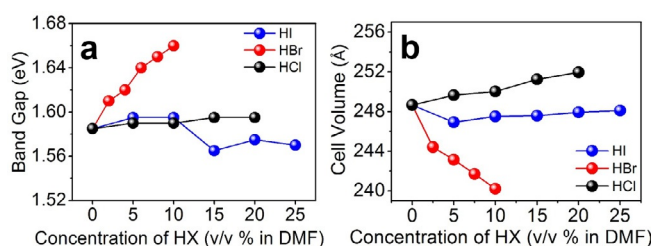


Figure 6. Compiled (a) optical bandgaps and (b) cell volumes of the perovskite films as a function of HX additive concentration used in film preparation. The cell volumes are extrapolated from the PXRD data of the corresponding thin films on ITO/PEDOT:PSS substrates using Jana2006 Software.^[51]

tional theory (DFT) calculations,^[53] although the change is more subtle in our study. Regarding volume effects, our data show a negligible change in cell volume upon phase transition, whereas the temperature-dependent structural data^[37] reveal unit cell volume contraction as the perovskite structure evolves from tetragonal to cubic upon thermal activation, thereby opening the $\text{M}-\text{X}-\text{M}$ angle and affording a more compact unit cell. We rationalize this disparity by attributing the change in bandgap solely to the change in the $[\text{PbI}_3]^-$ octahedral tilting without affecting the volume. Furthermore, the difference in the mechanism of cubic phase formation through thermal activation versus HX addition can plausibly explain the observed volume–bandgap– I^- trends. The present findings of a slight red-shift in the bandgap at high HI concentrations can be rationalized by regulation of the I^- content, which should have the maximum density of iodide defects within a Schottky-type defect model (see below). In this system, HI addition regulates the I^- content, and filling of iodide vacancies dominates at high HI concentrations. As a result, these shallow defects smear out, affording a thin film bandgap corresponding to that of the bulk perovskite.

(b) HBr. The HBr case is similarly straightforward. Br^- can be incorporated into the perovskite structure by substituting for some I^- ions and forming a genuine solid solution.^[4,30,36,54] When I^- is replaced by Br^- , the cell volume is expected to contract and the bandgap to increase due to the smaller size of Br^- . This trend agrees with the present data showing a gradual fall in cell volume and opening of the bandgap as the HBr con-

centration in the precursor solution is increased. Note that Br^- contents as low as 2.5 vol% are sufficient to form a solid solution retaining the perovskite tetragonal structure. However, starting from approximately 5 vol% HBr, there is sufficient Br^- to induce the tetragonal→cubic transition. In principle, at 10 vol% HBr, the Br/I molar ratio from the stoichiometric iodide precursor solution should be 1:3, corresponding to the composition $\text{CH}_3\text{NH}_3\text{PbI}_{2.25}\text{Br}_{0.75}$ in an ideal scenario where all available Br^- is incorporated into the crystal structure. To assay the actual Br^- incorporation, the bandgap is plotted versus x for the $\text{CH}_3\text{NH}_3\text{PbI}_{3-x}\text{Br}_x$ thin film data ($x=0, 1, 1.5, 2, 3$) as shown in Figure S6, and the linearity confirms Vegard's law behavior. The $\text{CH}_3\text{NH}_3\text{PbI}_3$ thin film has a bandgap of 1.59 eV, whereas that of $\text{CH}_3\text{NH}_3\text{PbBr}_3$ is 2.27 eV. From this linear relationship, the Br^- content across the $\text{CH}_3\text{NH}_3\text{PbI}_{3-x}\text{Br}_x$ film series can be estimated. For 10 vol% HBr film, the Br^- content in the film is determined to be 13.4%, roughly one-half of the Br^- amount in the solution concentration (~25%). This result shows that the film is Br^- -deficient versus the Br^- content of the precursor solution; that is, HBr shifts the equilibrium towards incorporation of I^- in the perovskite film versus that in pure DMF solutions.^[55] Note that this observation applies only to thin-film fabrication with HBr-containing precursor solutions, and not to bulk material synthesis; when the perovskite crystals are synthesized from stoichiometric $\text{CH}_3\text{NH}_3\text{I} + \text{PbI}_2$ in an HBr-only precursor solution, it is found that the Br/I ratio is small, with the heavy halide dominating and precipitation of the all- I^- perovskite.

(c) HCl. Unlike the case of HBr, the large Cl^- versus I^- ionic radius disparity disfavors solid solution formation. However, the observed changes in lattice parameters from the data refinement (Figure 3c) suggest that some alterations in the $\text{CH}_3\text{NH}_3\text{PbI}_3$ structure are in fact induced by HCl. Unlike the case of HI or HBr, in the HCl system, the cubic phase is observed when the unit cell volume is large, and the bandgap only marginally changed. To probe the compositions in detail, time-of-flight secondary ion mass spectrometry (ToF-SIMS) analysis was performed on the HCl-treated $\text{CH}_3\text{NH}_3\text{PbI}_3$ thin films to assay the composition at the film surfaces and in the film bulk (Figure S7a). From Figure S7b, it is concluded that there is a negligible Cl^- incorporation in the perovskite lattice, as expected from the crystal structure analysis. This is because Cl^- incorporation would contract the unit cell parameters as in

the HBr case discussed above, which is not observed. The origin of the bandgap and cell volume change in the HCl-treated films is intriguing. However, this effect cannot be directly attributed to Cl^- incorporation for the structure/composition reasons discussed. A possible explanation of this effect is discussed in the sections below.

To explore any chlorine-doping effects in HCl-treated films compared to the 3:1 $\text{CH}_3\text{NH}_3\text{I}/\text{PbCl}_2$ method, solar cell device performance was next compared for the HCl-treated and $\text{CH}_3\text{NH}_3\text{PbI}_{3-x}\text{Cl}_x$ films in planar heterojunction device structures, ITO/PEDOT:PSS/perovskite/PCBM/PEI/Au, where PCBM is phenyl-C61-butyric acid methyl ester, and PEI is poly(ethyleneimine). As shown in Figure S8, the solar cell parameters improve significantly when HCl is used as an additive, likely because of the drastic enhancement in perovskite film morphology. In a series with HCl concentration varying from 5–20 vol%, the optimal PCE is obtained with 10% HCl, affording open-circuit voltage (V_{OC}) = 0.897 V, short-circuit current density (J_{SC}) = 20.81 mA cm^{-2} , fill factor (FF) = 55.02%, and consequently PCE = 10.3%, comparable to that of $\text{CH}_3\text{NH}_3\text{PbI}_{3-x}\text{Cl}_x$ films prepared from 3:1 $\text{CH}_3\text{NH}_3\text{I}/\text{PbCl}_2$ precursor solutions as shown in Table S1. The similarity in PV performance between the 10 vol% HCl and $\text{CH}_3\text{NH}_3\text{PbI}_{3-x}\text{Cl}_x$ systems suggests that the quality of these perovskite films with acidic additives is clearly superior, thereby achieving comparable PCEs.

The effects of HX additives—A hypothesis

The observed changes in optical bandgap and cell lattice as well as unusual room-temperature tetragonal \rightarrow cubic phase transition cannot be explained by thermal activation effects alone. We hypothesize that the optical and structural changes are induced by the changes in the structure arising from Schottky disorder^[56] in the perovskite polycrystalline thin films while the phase transition is correlated with the structural strain induced upon HX addition when the crystallites are in the μm range or less. This is a well-documented phenomenon for perovskites. For example, in BaTiO_3 , a reduction in grain size depresses the tetragonal \rightarrow cubic phase transformation from that of the bulk material, 120 \rightarrow 25 $^\circ\text{C}$.^[57–59] In single crystals or large grains of crystallites, the number of the crystal structure repeat units is large, and large grains are generally unstressed.^[57–59] While the present acid additives dramatically enhance perovskite film coverage by producing small crystallites with a more uniform size distribution, they also affect the surface energy of each individual crystallite, resulting in the

breakup of larger crystallite aggregates into small crystallites with greater surface/volume ratios (Figure 2), thus increasing the overall surface energy. Such changes in surface energy are unavoidably accompanied by a substantial increase in lattice strain, inducing lattice defects in the perovskite.^[58] Such a phenomenon was recently reported by Eperon et al. where they observed a phase transition in the inorganic CsPbI_3 perovskite system from a yellow wide-bandgap orthorhombic phase to a black cubic phase upon HI addition, and strain introduced in the crystal lattice upon formation of small grains was ascribed to the observed phase transition.^[31] Our hypothesis for the $\text{CH}_3\text{NH}_3\text{PbI}_3$ system in the present work is in excellent agreement with the observations in both BaTiO_3 and CsPbI_3 systems.

The nature of defects in $\text{CH}_3\text{NH}_3\text{PbI}_3$ is considered anomalous because this material exhibits unusually low free-carrier concentrations despite the low formation energy of defects, typically observed only in wide-bandgap materials.^[56] Walsh et al. explained this behavior by proposing a mechanism whereby ionic compensation is achieved by “self-regulation” of carrier concentrations through Schottky defect formation enabled by the low lattice energy and low metal oxidation states generally found in halide versus oxide perovskites.^[56] Note that there are two possible types of point defects, namely Schottky and Frenkel. A Schottky defect is a stoichiometric defect with equal numbers of cationic and anionic point defects (vacancies) that compensate each other; thus, the crystal composition is unchanged and charge-balanced. Nevertheless, the presence of small densities of such defects can substantially alter materials properties.^[60] Most alkali halides and alkaline earth oxides possess predominantly Schottky defects. In contrast, Frenkel defects are created when ions move to interstitial sites where they are stabilized by the opposite charges of neighboring ions, generating point charged defects. Frenkel defects with elemental vacancies are known to be associated with unintentional doping of perovskite: CH_3NH_3^+ and Pb^{2+} vacancies for p-type doping and I^- vacancies for n-type doping.^[61] However, if present in large quantities in halide perovskites, such Frenkel defects should lead to high electrical conductivity, which is not observed.^[36] Therefore, Schottky defects, either full or partial, are considered to dominate in halide perovskites owing to the partially ionic nature of the Pb-X bonds and the electrostatic interaction between CH_3NH_3^+ cations and the PbX_3^- lattice.^[4,56,61–63] In this model the perovskite is overall neutrally charged because of self-compensation of cationic and anionic point defects, consistent with the observed benign electronic nature of this material.

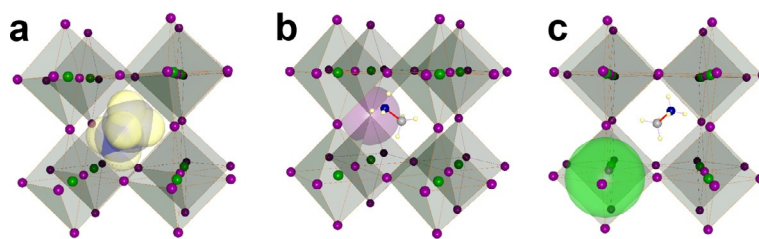


Figure 7. Graphical representation of the $\text{CH}_3\text{NH}_3\text{PbI}_3$ perovskite crystal structure with (a) CH_3NH_3^+ vacancies, (b) I^- vacancies, and (c) Pb^{2+} vacancies. The color coding indicates the location of the vacancy.

To explain the aforementioned phase transitions in the present materials as well as changes in optical properties and lattice expansion/compression, we consider a defect model in which Schottky defects are dominant, supported by the DFT study of Wei and coworkers.^[56] These calculations show that the Schottky defect formation energy is very low in hybrid halide perovskites, 0.14 eV versus 2.29 eV per defect in BaTiO₃. The partial Schottky formation energies of CH₃NH₃I and PbI₂ vacancies are 0.08 eV and 0.22 eV, respectively, at 25 °C. The favored defect is CH₃NH₃I with a strikingly low formation energy; therefore, a plausible level of the CH₃NH₃⁺ and I⁻ sublattices as high as 4% can be unoccupied at 25 °C.^[56] We hypothesize that introducing HX additives to perovskites enables self-regulation of lattice vacancies (Figure 7) by providing extra X⁻ and H⁺ ions that regenerate CH₃NH₃⁺ and I⁻, thereby inducing changes in volume, M–X–M coupling, and the optical bandgap.

Assuming that the perovskite vacancies are predominantly at halide sites adjacent to Pb²⁺, X⁻ anions should ion-exchange/occupy the vacant sites. This possibility is realistic in solution-processed thin films because the crystallization occurs very rapidly, thereby facilitating defect formation. Within this model, all halide ions are good candidates to occupy these positions. The effect, however, is slightly different in each case: i) for HI, I⁻ ions occupy the vacant sites, restoring the Pb–I–Pb connectivity of the [PbI₃]⁻ network. As a result, the perovskite bandgap decreases, resembling that of the bulk material; ii) for HBr, the effect is similar as the Br⁻ ionic size is sufficient to restore the perovskite lattice, forming a [PbI_{3-x}Br_x]⁻ network, which is confirmed here experimentally in the bandgaps of the CH₃NH₃PbI_{3-x}Br_x solid solutions; iii) for HCl, the Cl⁻ ions cannot form solid solutions unlike Br⁻ due to the disparate Cl⁻ and I⁻ ionic radii. However, it is possible that small amounts of Cl⁻ participate in the perovskite framework by coordinating to either metal ions, forming Pb–Cl–Pb dangling bonds or form loosely bound Pb–Cl–Pb ion pairs. This picture is consistent with the slight increase in unit cell volume because the repulsive ion-pair interactions may account for such an effect while at the same time providing a model for widening of the bandgap. At this point, this working hypothesis serves as a reasonable conceptual model to interpret the experimental results. Nevertheless, further studies, both theoretical and experimental, will be required to define the limits of this model and are currently underway.

Conclusions

A detailed structural, optical spectroscopic, and photovoltaic study of the effects of a series of hydrohalic acid (HX, X=I, Br, Cl) additives on methylammonium lead iodide perovskite (CH₃NH₃PbI₃) film properties reveals that all three acids affect the optical properties and alter the unit cell lattice parameters. These changes are subtle and can be understood by correlating them with the types of defects present in the polycrystalline thin films and the strain induced in the structures of very small crystallites. Remarkably, a room temperature tetragonal–cubic phase transition is observed for CH₃NH₃PbI₃ thin

films at high HX concentrations. Further insights into this surprising phase transformation are obtained from in situ variable-temperature X-ray diffraction over the 25–55 °C (298–328 K) range, demonstrating a decline in transition temperature with increasing acid concentration. This phase transition provides indirect evidence for the presence of intrinsic defects in CH₃NH₃PbI₃, where the HX additives induce “self-healing” by providing extra halide and CH₃NH₃⁺ (regenerated from the CH₃NH₂ and extra H⁺) that regulate the Schottky defect formation during perovskite crystallization. The acids, acting as proton sources, also modify the precursor solution equilibria, a factor that significantly affects the chemical composition of the perovskite films. Furthermore, these additives have a striking impact on the crystallization rate and film formation by dramatically enhancing film morphology and surface coverage. Therefore, the present study provides a springboard for further exploration of defects in halide perovskites, as they can be studied in greater detail through tuning the proper selection of additives.

Experimental Section

Materials. Unless otherwise stated, all reagents were purchased from Sigma–Aldrich and used without further purification. PEDOT:PSS and PC₆₁BM (purity > 99%) were obtained from Clevios and American Dye Source Inc., respectively.

Substrate cleaning. The patterned ITO-coated glass (145 nm, 20 Ω □⁻¹, Thin Film Devices Inc.) or microscope glass or Si/SiO₂ substrates were cleaned by sequential sonication at 50 °C in aqueous detergent, deionized water, methanol (MeOH), isopropanol (IPA), and acetone (ACE) for 15 min each. Substrates were blown dry with nitrogen after each solvent wash. Just prior to device fabrication, the pre-cleaned substrates were further sonicated in ACE, followed by a 15 min UV ozone (Jelight Inc., Model 42) treatment.

Perovskite Film Fabrication. A 0.88 M stock solution of CH₃NH₃PbI₃ was prepared by mixing CH₃NH₃I and PbI₂ in a 1:1 stoichiometric ratio in anhydrous DMF (99.8%) at 100 °C to ensure complete dissolution. The solution was then cooled to 70 °C and filtered through a 0.45 μm Nylon filter. The concentration of HX [57 wt% HI, 46 wt% HBr, 37 wt% HCl in H₂O, or deionized H₂O (control)] in the precursor solution was varied by adding measured amounts of the acid/water to the stock CH₃NH₃PbI₃ solution (2.5–25 vol%) just prior to spin-coating the solution. A perovskite layer was fabricated by spin-coating the as-prepared solution with varied HX concentrations (vol%) on ITO/PEDOT:PSS, glass, or Si/SiO₂ substrates at 2000 rpm for 30 s, followed by annealing at 100 °C for 2 min in a dry box with < 3% relative humidity.

Film Characterization. SEM images were obtained using a field emission SEM (Hitachi SU8030) equipped with an electron beam accelerated at 500 V–30 kV. AFM images were acquired using a scanning probe microscope (Bruker ICON System) in the tapping mode. The PXRD measurements were carried out on a Rigaku Mini-Flex600 X-ray diffractometer (CuKα radiation, λ = 1.5406 Å) operating at 40 kV and 15 mA. Samples for SEM, AFM, and PXRD measurements were prepared on ITO/PEDOT:PSS substrates. GIWAXS measurements were performed at Beamline 8-ID-E of the Advanced Photon Source at Argonne National Laboratory. Samples were exposed to an X-ray beam (λ = 1.6868 Å) at an incident angle

of 0.20° for 5 summed 4 s exposures totaling 20 s of X-ray exposure, and the scattered light was collected by a Pilatus 1 m pixel array detector at 204 mm from the sample. A Shimadzu UV-3600 double-beam, double-monochromator spectrophotometer was used to acquire room-temperature optical diffuse reflectance spectra in the range of 200–2500 nm. BaSO₄ was used as a non-absorbing reflectance reference, and reflectance data were converted to absorbance values using the Kubelka–Munk transformation. ToF-SIMS was conducted on a PHI TRIFT III (Physical Electronics Inc.). The bulk effect was studied by etching the first few nm of the surface with an incident Ga ion beam. For better accuracy, the Cl⁻ content in the acid-treated films was calculated by the ratio between the counts from Cl⁻ and the total counts of Cl⁻ and I⁻.

XRD pattern matching. Lattice parameters were determined by matching XRD patterns of the two-phase systems, keeping the peak position of the ITO reflections fixed to the value obtained from the blank ITO/PEDOT:PSS substrate and refining the instrumental shift along with the perovskite lattice parameters for a pseudo-Voigt peak fitting model.

In situ variable-temperature XRD. X-ray reflectivity θ – 2θ scans were performed on a Rigaku Smartlab instrument at a CuK α radiation wavelength of $\lambda = 1.541 \text{ \AA}$ with an Anton Paar DHS 1100 heating stage. Temperature was incremented in a stepwise manner and allowed to stabilize before data acquisition. Poisson counting error bars were used in fitting observed peaks to Gaussian function.

Solar Cell Device Fabrication. Approximately 40 nm of PEDOT:PSS was deposited on clean ITO substrates by spin-coating at 6000 rpm for 30 s and annealed at 160 °C for 15 min in air. The substrates were then transferred to a dry box with <5% relative humidity and dried again at 100 °C for 30 min to remove any adsorbed water. Perovskite films were deposited as described above. Thin layers of PC₆₁BM and PEI were sequentially deposited on the perovskite film from a 20 mg mL⁻¹ PC₆₁BM solution in chlorobenzene (anhydrous, 99.8%) and a solution of poly(ethyleneimine) in anhydrous IPA at 1000 rpm and 3000 rpm, respectively, under inert atmosphere. The contact area for the metal electrode was defined by etching the perovskite layer with a cotton swab soaked with acetonitrile. Finally, 80 nm of Au (99.99%) was thermally evaporated through a shadow mask at a pressure of $\sim 5 \times 10^{-6}$ torr, affording four devices per substrate. The device area was 0.065 cm².

Solar Cell Device Characterization. The current density versus voltage (J – V) data were collected in air without any encapsulation using a Keithley 2400 source meter under simulated AM1.5G irradiation (100 mW cm⁻²) generated by Spectra-Nova Class A solar simulator. The light intensity was calibrated by using an NREL-certified KG3-filtered Si reference cell to reduce the spectral mismatch.

Acknowledgements

This work was supported as part of the ANSER Center, an Energy Frontier Research Center funded by the U.S. Department of Energy, Office of Science, Office of Basic Energy Sciences, under award number DE-SC0001059. This work made use of the J. B. Cohen X-Ray Diffraction Facility supported by the MRSEC program of the National Science Foundation (DMR-1121262) at the Materials Research Center of Northwestern University. Electron microscopy and ToF-SIMS measurements were performed at the

Electron Probe Instrumentation Center (EPIC) and at the Keck-II facility of NUANCE Center, respectively, at Northwestern University. The NUANCE Center is supported by the International Institute for Nanotechnology, the Northwestern University MRSEC (NSF DMR-1121262), the Keck Foundation, the State of Illinois, and Northwestern University. Use of the Advanced Photon Source, an Office of Science User Facility operated for the U.S. Department of Energy (DOE) Office of Science by Argonne National Laboratory, was supported by the U.S. DOE under Contract No. DE-AC02-06CH11357. We thank Dr. X. Chen for help with ToF-SIMS measurements and Mr. N. D. Eastham for assistance with AFM. We also thank Dr. H.-C. Liao, Dr. K. Lim, and Dr. T.-B. Song for helpful discussions.

Keywords: additives · perovskite · phase transition · thin films · x-ray diffraction

- [1] S. Kazim, M. K. Nazeeruddin, M. Grätzel, S. Ahmad, *Angew. Chem. Int. Ed.* **2014**, *53*, 2812–2824; *Angew. Chem.* **2014**, *126*, 2854–2867.
- [2] N.-G. Park, *J. Phys. Chem. Lett.* **2013**, *4*, 2423–2429.
- [3] M. A. Green, A. Ho-Baillie, H. J. Snaith, *Nat. Photonics* **2014**, *8*, 506–514.
- [4] C. C. Stoumpos, M. G. Kanatzidis, *Acc. Chem. Res.* **2015**, *48*, 2791–2802.
- [5] T. C. Sum, N. Mathews, *Energy Environ. Sci.* **2014**, *7*, 2518–2534.
- [6] G. Xing, N. Mathews, S. Sun, S. S. Lim, Y. M. Lam, M. Grätzel, S. Mhaisalkar, T. C. Sum, *Science* **2013**, *342*, 344–347.
- [7] S. D. Stranks, G. E. Eperon, G. Grancini, C. Menelaou, M. J. Alcocer, T. Leijtens, L. M. Herz, A. Petrozza, H. J. Snaith, *Science* **2013**, *342*, 341–344.
- [8] P. Gao, M. Grätzel, M. K. Nazeeruddin, *Energy Environ. Sci.* **2014**, *7*, 2448.
- [9] H.-S. Kim, C.-R. Lee, J.-H. Im, K.-B. Lee, T. Moehl, A. Marchioro, S.-J. Moon, R. Humphry-Baker, J.-H. Yum, J. E. Moser, M. Grätzel, N.-G. Park, *Sci. Rep.* **2012**, *2*, 591.
- [10] J. H. Heo, S. H. Im, J. H. Noh, T. N. Mandal, C.-S. Lim, J. A. Chang, Y. H. Lee, H.-j. Kim, A. Sarkar, K. Nazeeruddin, M. Grätzel, S. I. Seok, *Nat. Photonics* **2013**, *7*, 486–491.
- [11] M. M. Lee, J. Teuscher, T. Miyasaka, T. N. Murakami, H. J. Snaith, *Science* **2012**, *338*, 643–647.
- [12] H. S. Jung, N.-G. Park, *Small* **2015**, *11*, 10–25.
- [13] Y. Lee, D. B. Mitzi, P. W. Barnes, T. Vogt, *Phys. Rev. B* **2003**, *68*, 020103.
- [14] Q. Chen, H. Zhou, Z. Hong, S. Luo, H.-S. Duan, H.-H. Wang, Y. Liu, G. Li, Y. Yang, *J. Am. Chem. Soc.* **2014**, *136*, 622–625.
- [15] F. Hao, C. C. Stoumpos, Z. Liu, R. P. Chang, M. G. Kanatzidis, *J. Am. Chem. Soc.* **2014**, *136*, 16411–16419.
- [16] J. Burschka, N. Pellet, S.-J. Moon, R. Humphry-Baker, P. Gao, M. K. Nazeeruddin, M. Grätzel, *Nature* **2013**, *499*, 316–319.
- [17] M. Liu, M. B. Johnston, H. J. Snaith, *Nature* **2013**, *501*, 395–398.
- [18] W. Nie, H. Tsai, R. Asadpour, J.-C. Blancon, A. J. Neukirch, G. Gupta, J. J. Crochet, M. Chhowalla, S. Tretiak, M. A. Alam, H.-L. Wang, A. D. Mohite, *Science* **2015**, *347*, 522–525.
- [19] P. Docampo, J. M. Ball, M. Darwich, G. E. Eperon, H. J. Snaith, *Nat. Commun.* **2013**, *4*, 2761.
- [20] N. J. Jeon, J. H. Noh, W. S. Yang, Y. C. Kim, S. Ryu, J. Seo, S. I. Seok, *Nature* **2015**, *517*, 476–480.
- [21] H.-B. Kim, H. Choi, J. Jeong, S. Kim, B. Walker, S. Song, J. Y. Kim, *Nanoscale* **2014**, *6*, 6679–6683.
- [22] N. J. Jeon, J. H. Noh, Y. C. Kim, W. S. Yang, S. Ryu, S. I. Seok, *Nat. Mater.* **2014**, *13*, 897–903.
- [23] M. Xiao, F. Huang, W. Huang, Y. Dkhissi, Y. Zhu, J. Etheridge, A. Gray-Weale, U. Bach, Y.-B. Cheng, L. Spiccia, *Angew. Chem.* **2014**, *126*, 10056–10061.
- [24] A. Dualeh, N. Tétreault, T. Moehl, P. Gao, M. K. Nazeeruddin, M. Grätzel, *Adv. Funct. Mater.* **2014**, *24*, 3250–3258.
- [25] G. E. Eperon, V. M. Burlakov, P. Docampo, A. Goriely, H. J. Snaith, *Adv. Funct. Mater.* **2014**, *24*, 151–157.
- [26] P.-W. Liang, C.-Y. Liao, C.-C. Chueh, F. Zuo, S. T. Williams, X.-K. Xin, J. Lin, A. K. Y. Jen, *Adv. Mater.* **2014**, *26*, 3748–3754.

- [27] C.-C. Chen, Z. Hong, G. Li, Q. Chen, H. Zhou, Y. Yang, *J. Photonics Energy* **2015**, *5*, 057405.
- [28] Y. Zhao, K. Zhu, *J. Phys. Chem. C* **2014**, *118*, 9412–9418.
- [29] C. Zuo, L. Ding, *Nanoscale* **2014**, *6*, 9935–9938.
- [30] G. E. Eperon, S. D. Stranks, C. Menelaou, M. B. Johnston, L. M. Herz, H. J. Snaith, *Energy Environ. Sci.* **2014**, *7*, 982.
- [31] G. E. Eperon, G. M. Paterno, R. J. Sutton, A. Zampetti, A. A. Haghighirad, F. Cacialli, H. J. Snaith, *J. Mater. Chem. A* **2015**, *3*, 19688–19695.
- [32] G. Li, T. Zhang, Y. Zhao, *J. Mater. Chem. A* **2015**, *3*, 19674–19678.
- [33] F. Wang, H. Yu, H. Xu, N. Zhao, *Adv. Funct. Mater.* **2015**, *25*, 1120–1126.
- [34] N. Onoda-Yamamuro, O. Yamamuro, T. Matsuo, H. Suga, *J. Phys. Chem. Solids* **1992**, *53*, 277–281.
- [35] R. L. Milot, G. E. Eperon, H. J. Snaith, M. B. Johnston, L. M. Herz, *Adv. Funct. Mater.* **2015**, *25*, 6218–6227.
- [36] C. C. Stoumpos, C. D. Malliakas, M. G. Kanatzidis, *Inorg. Chem.* **2013**, *52*, 9019–9038.
- [37] A. Poglitsch, D. Weber, *J. Chem. Phys.* **1987**, *87*, 6373–6378.
- [38] Y. Wang, X. Lu, W. Yang, T. Wen, L. Yang, X. Ren, L. Wang, Z. Lin, Y. Zhao, *J. Am. Chem. Soc.* **2015**, *137*, 11144–11149.
- [39] N. Onoda-Yamamuro, T. Matsuo, H. Suga, *J. Phys. Chem. Solids* **1990**, *51*, 1383–1395.
- [40] T. Baikie, Y. Fang, J. M. Kadro, M. Schreyer, F. Wei, S. G. Mhaisalkar, M. Graetzel, T. J. White, *J. Mater. Chem. A* **2013**, *1*, 5628.
- [41] O. Knop, R. E. Wasylishen, M. A. White, T. S. Cameron, M. J. M. V. Oort, *Can. J. Chem.* **1990**, *68*, 412–422.
- [42] Q. Xu, T. Eguchi, H. Nakayama, N. Nakamura, M. Kishita, *Z. Naturforsch. A* **1991**, *46*, 240.
- [43] D. H. Fabini, T. Hogan, H. A. Evans, C. C. Stoumpos, M. G. Kanatzidis, R. Seshadri, *J. Phys. Chem. Lett.* **2016**, *7*, 376–381.
- [44] T.-B. Song, Q. Chen, H. Zhou, C. Jiang, H.-H. Wang, Y. Yang, Y. Liu, J. You, Y. Yang, *J. Mater. Chem. A* **2015**, *3*, 9032–9050.
- [45] Q. Wang, Y. Shao, Q. Dong, Z. Xiao, Y. Yuan, J. Huang, *Energy Environ. Sci.* **2014**, *7*, 2359–2365.
- [46] Y. Guo, K. Shoyama, W. Sato, Y. Matsuo, K. Inoue, K. Harano, C. Liu, H. Tanaka, E. Nakamura, *J. Am. Chem. Soc.* **2015**, *137*, 15907–15914.
- [47] D. H. Cao, C. C. Stoumpos, C. D. Malliakas, M. J. Katz, O. K. Farha, J. T. Hupp, M. G. Kanatzidis, *APL Mater.* **2014**, *2*, 091101.
- [48] J. Borchert, H. Boht, W. Franzel, R. Csuk, R. Scheer, P. Pistor, *J. Mater. Chem. A* **2015**, *3*, 19842–19849.
- [49] Q. Wang, M. Lyu, M. Zhang, J. H. Yun, H. Chen, L. Wang, *J. Phys. Chem. Lett.* **2015**, *6*, 4379–4384.
- [50] F. Hao, C. C. Stoumpos, P. Guo, N. Zhou, T. J. Marks, R. P. H. Chang, M. G. Kanatzidis, *J. Am. Chem. Soc.* **2015**, *137*, 11445–11452.
- [51] V. Petříček, M. Dušek, L. Palatinus in *Zeitschrift für Kristallographie–Crystalline Materials*, **2014**, *229*, 345–352.
- [52] J. Im, C. C. Stoumpos, H. Jin, A. J. Freeman, M. G. Kanatzidis, *J. Phys. Chem. Lett.* **2015**, *6*, 3503–3509.
- [53] C. Quarti, E. Mosconi, J. M. Ball, V. D’Innocenzo, C. Tao, S. Pathak, H. J. Snaith, A. Petrozza, F. De Angelis, *Energy Environ. Sci.* **2016**, *9*, 155–163.
- [54] J. H. Noh, S. H. Im, J. H. Heo, T. N. Mandal, S. I. Seok, *Nano Lett.* **2013**, *13*, 1764–1769.
- [55] S. J. Yoon, K. G. Stamplecoskie, P. V. Kamat, *J. Phys. Chem. Lett.* **2016**, *7*, 1368–1373.
- [56] A. Walsh, D. O. Scanlon, S. Chen, X. G. Gong, S. H. Wei, *Angew. Chem. Int. Ed.* **2015**, *54*, 1791–1794; *Angew. Chem.* **2015**, *127*, 1811–1814.
- [57] G. Arlt, D. Hennings, G. de With, *J. Appl. Phys.* **1985**, *58*, 1619–1625.
- [58] B. D. Begg, E. R. Vance, J. Nowotny, *J. Am. Ceram. Soc.* **1994**, *77*, 3186–3192.
- [59] M. H. Frey, D. A. Payne, *Phys. Rev. B* **1996**, *54*, 3158–3168.
- [60] A. R. West, *Solid State Chemistry and its Applications*, 2nd ed., Wiley, **2014**.
- [61] J. Kim, S.-H. Lee, J. H. Lee, K.-H. Hong, *J. Phys. Chem. Lett.* **2014**, *5*, 1312–1317.
- [62] J.-H. Yang, W.-J. Yin, J.-S. Park, S.-H. Wei, *Sci. Rep.* **2015**, *5*, 16977.
- [63] W.-J. Yin, T. Shi, Y. Yan, *Appl. Phys. Lett.* **2014**, *104*, 063903.

Received: July 3, 2016

Revised: August 15, 2016

Published online on September 15, 2016